

Determination of Gallium Concentration in Silicon from Low-Temperature Photoluminescence Analysis

Tarek O. Abdul Fattah,* Janet Jacobs, Vladimir P. Markevich, Nikolay V. Abrosimov, Ian D. Hawkins, Matthew P. Halsall, Iain F. Crowe, and Anthony R. Peaker

Increasing the understanding of the electronic properties of gallium (Ga) in silicon (Si) used nowadays to manufacture p-type Si solar cells is of key technological importance. In this contribution, the results of the effect of Ga concentration on the low-temperature photoluminescence (PL) spectra in crystalline Si are reported. The Ga-doped Si samples studied have negligible boron concentrations, which can complicate spectral analysis of the bound exciton (BE) lines. The split Ga BE ground state at $T = 10\text{ K}$ is analyzed and the PL intensity ratios for the BE to free exciton peaks are compared. By comparing these to known Ga concentrations, derived from capacitance–voltage measurements, an all-optical (PL) calibration curve for the quantification of Ga concentration in Si is established. The effects of both temperature and excitation power on the PL intensity ratios are also studied. By combining the temperature-induced changes in the PL intensity ratios with the calibration curve at 10 K, a calibration function has been determined. It is found that the decay rates of the PL intensity ratios as a function of excitation power are independent of the chosen (split) BE peak. The major benefits of this method and its limitations are discussed.

1. Introduction

The progressive replacement of boron (B) by gallium (Ga) as the choice acceptor impurity for the fabrication of the p-type base layer in silicon (Si) solar cells brings with it the need to fully understand the electronic (and chemical) properties of Ga in Si, so as to facilitate characterization of this relatively new solar cell material.^[1–3] The ability to measure impurity properties is of particular importance in determining their effects on wafer

quality, charge carrier transport, reliability, device performance, and degradation.

The use of low-temperature photoluminescence (PL) on Si has a long history of success in investigating impurities. This is because recording PL on samples is relatively fast, processing of samples for measurements is not difficult, and the technique is highly sensitive. Unfortunately, precise quantification of, say, impurity concentration represents a challenge as there are a multiplicity of factors that govern the optical activity of a particular impurity and thus the observed PL intensity associated with it. One convenient approach to this is the standard technique of comparing the ratio of intensities of a particular impurity-related PL emission line with that of an intrinsic PL feature, such as the free exciton (FE) line. This almost completely eradicates the effect of many of the variables on either emission feature, within the same

sample, providing a meaningful quantification of the impurity concentration. A comprehensive review of the effect of impurity concentration on the low temperature PL spectra of Si was recently published.^[4]

After being first proposed by Tajima et al.^[5] the use of PL to determine impurity concentration in this way was standardized as a technique to quantify donor and acceptor impurities in Si (Japanese Industrial Standard,^[6] Semiconductor Equipment and Materials International,^[7] and American Standards for Testing and Materials^[8]).

This technique has been shown to be preferred to many others used in the semiconductor field to conduct similar analysis. For instance, conventional room temperature resistivity measurements with the help of the Irvin curve^[9] cannot determine the precise impurity species and compensation ratio. Temperature-dependent Hall effect measurements suffer from the difficulty of processing and analyzing samples with relatively high resistivity.^[10,11] Secondary ion mass spectroscopy (SIMS) is a destructive technique and has poor detectivity for some, notably light, elements and is generally more challenging for the reliable study of impurity concentrations in the range $10^{13} – 10^{14}\text{ cm}^{-3}$. In contrast, PL can reveal not only the presence of specific impurities at very low concentrations, but also the mechanism by which the radiative transition associated with it proceeds, e.g., via electron/hole transitions between impurity-related energy levels and conduction/vacuum bands, without the requirement for

T. O. Abdul Fattah, J. Jacobs, V. P. Markevich, I. D. Hawkins, M. P. Halsall, I. F. Crowe, A. R. Peaker
Photon Science Institute and Department of Electrical and Electronic Engineering (EEE)
University of Manchester
Manchester M13 9PL, UK
E-mail: tarek.abdulfattah@postgrad.manchester.ac.uk

N. V. Abrosimov
Leibniz-Institut für Kristallzüchtung (IKZ)
Max-Born-Straße 2, 12489 Berlin, Germany

 The ORCID identification number(s) for the author(s) of this article can be found under <https://doi.org/10.1002/solr.202300956>.

© 2023 The Authors. Solar RRL published by Wiley-VCH GmbH. This is an open access article under the terms of the Creative Commons Attribution License, which permits use, distribution and reproduction in any medium, provided the original work is properly cited.

DOI: [10.1002/solr.202300956](https://doi.org/10.1002/solr.202300956)

any sample processing (e.g., formation of electrical contacts). It is worth noting that the use of PL to derive impurity concentrations is not limited to Si. Indeed, it has also been applied to materials like cadmium telluride,^[12] ZnSe,^[13] Ge,^[14] and GaN.^[15,16]

The majority of published calibrations were derived from the transverse optical (TO) phonon-assisted BE (BE_{TO}) line,^[4] primarily because it tends to be the most intense PL feature for impurity-doped Si. However, as some studies have shown, it is equally valid to use the no-phonon (NP) BE line (BE_{NP}) relative to the transverse optical phonon-assisted FE line (FE_{TO}).^[17,18] Less common is the attempt to use the area of the NP line, as was reported by Colley and Lightowers, to generate calibration curves for B, phosphorus (P), and aluminum (Al) in Si,^[19] or the use of longitudinal acoustic (LA), rather than transverse acoustic (TA), phonon replicas, as was reported for impurities in Ge.^[14] The latter was likely motivated by the pronounced LA phonon replicas in Ge, which differs from Si where the NP and TO-phonon-assisted sidebands dominate the PL spectra.

Calibration curves covering wide concentration ranges, mostly for B and P species in Si, have been determined by several groups,^[19–21] although there are apparent inconsistencies in some of these reports.^[5,21,22] This is likely due to the varying experimental conditions and data treatments (measurement system response corrections or use of different luminescence features).^[19] The PL method was first applied on high resistivity Si materials with doping concentrations $< 10^{15} \text{ cm}^{-3}$ (for B and P)^[5] and on residual impurities in the low doping range $10^{12} – 10^{13} \text{ cm}^{-3}$ (for Al).^[17] The same method was applied to deduce the calibration data for P and arsenic (As), in epitaxially grown Si, for impurity concentrations in the range $10^{15} – 10^{16} \text{ cm}^{-3}$ and $10^{13} – 10^{16} \text{ cm}^{-3}$, respectively.^[18] Moreover, by calibrating against variable temperature Hall-effect measurements, not only were the P and B calibration curves determined, but an empirical equation, which describes the relationship between impurity concentration and PL intensity, was obtained.^[19] Al and As calibration curves were determined, with an accuracy of $\pm 30\%$, in 1990 by Tajima and co-workers, along with theoretical relations established for concentrations in the range $10^{12} – 10^{15} \text{ cm}^{-3}$.^[20] Later, to account for the higher doping concentrations that are commonly used in solar Si applications, the calibration curves for P and B were extended to 10^{17} cm^{-3} by PL measurements at 20 K.^[23] Similarly, the Al calibration curve for concentrations in the range $10^{15} – 10^{17} \text{ cm}^{-3}$ was determined from PL at 24 K.^[24] The feasibility of the technique was also examined near liquid nitrogen (N) temperatures (79 K) in the case of P and B on the basis that this temperature is more accessible to a wider range of laboratories.^[25] This type of PL impurity analysis has also been applied to establish the concentrations of other luminescent impurities. For instance, a method was proposed to determine the N concentration in Si by activating the Al–N luminescence center (A-line at 1.1223 eV) via Al⁺ implantation and annealing.^[26] Likewise, luminescence from radiation-induced defects, such as the C_i – C_s emission in Si (G-line at 0.969 eV), was shown to correlate with the carbon (C) concentration and as such can be used to quantify C contamination in Si, after electron irradiation treatments.^[27,28] A summary of all the reported calibration data in Si is provided in Table 1.

Surprisingly, and to the best of our knowledge, the calibration curve for Ga in Si has not yet been published, apart from some preliminary results by Schumacher and Whitney in 1986 for concentrations below $5 \times 10^{14} \text{ cm}^{-3}$.^[11] In that study, precise details regarding the TO-sideband of the Ga BE emission were omitted, although the issue of overlapping emission lines, e.g., as a result of B contamination, was identified. Further, at that time, access to very high-resolution PL measurements was limited, which might explain the absence of a reliable PL calibration curve for Ga in Si thus far. This motivates the application of high-resolution PL using modern spectroscopy instrumentation, and array detectors to investigate the luminescence features in Ga-doped Si to establish calibration data on Ga concentration. The determination of the relationship between the ratios of extrinsic to intrinsic PL lines and the Ga concentrations, which we report in this work, will allow researchers and industry alike to conduct impurity analysis on Ga-doped Si material used for solar PV applications.

2. Results and Discussion

Table 2 shows the Ga concentration in each of the studied samples as extracted from the acceptor concentration-depth, $N_A(W)$, profiles measured via C–V at room temperature on our Schottky diodes. These samples were cut from wafers coming from different parts of the grown ingots. Numbers in the first column of Table 2 will be used to refer to samples in the coming sections.

2.1. PL Spectrum of Ga-Doped Si at 10 K

Given that Ga-doped Si is considered as a relatively new material for wide scale implementation in the Si PV industry and the limited amount of work reported on it to date, it is important first to examine the luminescence features associated with the presence of Ga in Si. The normalized PL spectra, recorded at 10 K on Ga-doped Si samples, grown either by continuous Czochralski (CCz) or float zone (FZ) techniques, are depicted in Figure 1.

Similar to the case of well-studied B- and P-doped Si samples, the low-temperature PL spectrum of Ga-doped Si is composed of three well-resolved regions depending on the type of phonons involved in the radiative annihilation of acceptor bound excitons (BEs), which dominate the spectrum at this concentration level. Where the emission of phonons is combined with the process of radiative recombination, the overall energy of the emitted photon is reduced. This leads to an increase in observed photon energy when moving from the BE_{TO} phonon region to the BE_{TA} (BE_{TA}) region (consistent with the TO and TA phonon energies of ≈ 58 and ≈ 19 meV, respectively), and, further, to the NP BE_{NP} having the highest emission energy. The former is the most efficient phonon-assisted exciton annihilation channel in Si:Ga based on the selection rules for phonon assistance,^[29] while the latter also has a strong contribution in this case, unlike B-doped Si where the BE_{TO} transitions are much more efficient than the BE_{NP} ones.

The energetic positions of the Ga BE lines are slightly different from those related to B and P impurities in Si, which is due to differences in both the binding energy of excitons to Ga acceptors and the Ga ionization energy. Another effect clearly seen in

Table 1. Summary of the PL calibration curves of different impurities in Si available in the literature. The specific ratio and sample temperature used to produce the curve are shown.

Doping species	Height ratio used from PL	Concentration range [cm ⁻³]	Temperature [K]	References
Boron (B)	B(TO)/FE(TO)	$2.2 \times 10^{12} - 2.2 \times 10^{16}$	4.2 to 20	[39]
	B(TO)/FE(TO)	$1 \times 10^{13} - 1 \times 10^{15}$	—	[21]
	B(TO)/FE(TO)	$2 \times 10^{12} - 1 \times 10^{14}$	4.2	[11]
	B(TO)/FE(TO)	$5 \times 10^{14} - 5 \times 10^{17}$	20	[23]
	B(NP)/FE(TO)	$1 \times 10^{12} - 1 \times 10^{15}$	4.2	[19]
	B(TO)/FE(TO)	$5 \times 10^{15} - 5 \times 10^{17}$	79	[41]
	B(TO)/FE(TO)	$1 \times 10^{12} - 7 \times 10^{14}$	4.2	[5]
Phosphorus (P)	P(TO)/FE(TO)	$3.3 \times 10^{13} - 1 \times 10^{15}$	—	[21]
	P(TO)/FE(TO)	$1 \times 10^{12} - 1 \times 10^{16}$	4.2	[11]
	P(TO)/FE(TO)	$5 \times 10^{14} - 5 \times 10^{17}$	20	[23]
	P(NP)/FE(TO)	$1 \times 10^{12} - 2 \times 10^{15}$	4.2	[19]
	P(TO)/FE(TO)	$3 \times 10^{15} - 8 \times 10^{16}$	79	[41]
	P(TO)/FE(TO)	$3 \times 10^{11} - 8 \times 10^{14}$	4.2	[5]
	P(NP)/B(TO) ^{a)}	$2 \times 10^{15} - 2 \times 10^{16}$	4.2	[18]
Arsenic (As)	As(TO)/FE(TO)	$4 \times 10^{12} - 1 \times 10^{14}$	4.2	[20]
	As(NP)/B(NP) ^{a)}	$2 \times 10^{13} - 5 \times 10^{15}$	4.2	[18]
Aluminum (Al)	Al(TO)/FE(TO)	$5 \times 10^{12} - 2 \times 10^{15}$	4.2	[20]
	Al(NP)/FE(TO)	$1.8 \times 10^{12} - 1 \times 10^{13}$	—	[17]
	Al(TO)/FE(TO)	$1 \times 10^{15} - 1 \times 10^{17}$	24	[24]
	Al(NP)/FE(TO)	$7 \times 10^{13} - 2 \times 10^{15}$	4.2	[19]
Gallium (Ga)	Ga(TO)/FE(TO)	$7 \times 10^{13} - 4 \times 10^{14}$	4.2	[11]
Nitrogen (N)	A-line/FE(TO) ^{b)}	$4 \times 10^{13} - 2 \times 10^{15}$	4.2	[26]
Carbon (C)	G-line/FE(TO) ^{c)}	$1.4 \times 10^{14} - 3.6 \times 10^{15}$	4.2, 15 & 77	[28]

^{a)}Calibration curves determined for an epitaxially grown layer on B-doped Si substrate. ^{b)}A-line activated via Al implantation (dose of 1×10^{14} ions cm⁻², acceleration energy of 100 keV) at room temperature then annealed at 450 °C for 20 h. ^{c)}G-line activated via electron irradiation with an accelerating energy of 2 MeV and with multiple fluences.

Table 2. Details of the Ga-doped Si samples studied in this work.

Sample nos.	Ga concentration from C-V [cm ⁻³]	Growth technique
S1	$(9.6 \pm 0.12) \times 10^{14}$	FZ-Si
S2	$(1.62 \pm 0.13) \times 10^{15}$	FZ-Si
S3	$(3.95 \pm 0.21) \times 10^{15}$	FZ-Si
S4	$(6.9 \pm 0.25) \times 10^{15}$	FZ-Si
S5	$(7.23 \pm 0.3) \times 10^{15}$	CCz-Si
S6	$(1 \pm 0.25) \times 10^{16}$	FZ-Si
S7	$(1.05 \pm 0.27) \times 10^{16}$	CCz-Si
S8	$(1.32 \pm 0.28) \times 10^{16}$	CCz-Si
S9	$(3.45 \pm 0.39) \times 10^{16}$	CCz-Si

Figure 1 is that the Ga BE exhibits a triplet structure, with peaks labelled in Figure 1 as α , β , and γ , in order of increasing energy using the notation proposed in ref. [30]. For more details on the splitting of the Ga BE ground state, the reader is referred to refs. [30–32]. Note that a similar splitting of the BE ground state was also observed in Al-doped Si.^[33,34]

Note that at the temperature used to measure the data in Figure 1 (10 K), the intrinsic recombination channel is active and visible. This is very important as the most intense feature, the FE_{TO}, which is the basis of the calibration procedure used here, is completely quenched at liquid helium (He) temperatures for an impurity concentration around 10^{16} cm⁻³, as is commonly used in solar cells. This has been noted in previous works where higher temperatures were utilized to enhance the FE_{TO} peak^[23–25,35] at the expense of the acceptor BE emission.

2.2. Probing the Possibility of Contamination in the Studied Ga-Doped Si Samples

To produce the calibration curve, the extrinsic-to-intrinsic PL intensity ratio must be calibrated against a reliable method for the determination of the impurity concentration. C–V measurements are ubiquitously used in the semiconductor industry to depth profile the majority charge carrier concentration. Using this approach, the dopant impurity concentration is assumed to be equal to the majority carrier concentration (in this case, holes) based on the fact that the background concentration of

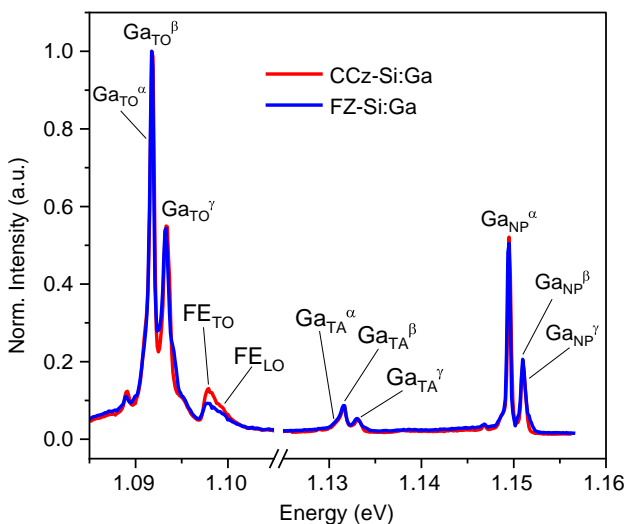


Figure 1. Normalized PL intensity of Ga-doped Si samples recorded at 10 K. Dominant luminescence lines are identified based on respective recombination channels with and without the involvement of phonons in the same notation used in.^[4,30] The presented spectra are recorded on samples s5 (CCz) and s6 (Fz) having Ga concentrations shown in Table 2.

compensating and codoped impurities is extremely low. Otherwise, the method would yield the net concentration $N_A - N_D$ (N_A and N_D are the total active acceptor and donor concentrations, respectively) instead of the absolute concentration of major dopant impurities in p-type Si. This is a particularly important consideration because at one time, before CCz growth was widely adopted, Ga doped ingots were often codoped with B. This was not the case with the samples we have used in this study.

Many of the calibration studies referenced here were performed under the assumption of negligible concentrations of compensating impurities (e.g., ref. [23]). Instead of making the same assumption and due to the important effect this would

have on the calibration curve, we have considered the contamination probability based on two methods: 1) temperature-dependent bias capacitance $C_b(T)$ measurements, and 2) low-temperature PL. Figure 2a shows the changes in C_b for Schottky diodes fabricated on a Ga-doped samples with different doping concentrations.

For temperatures above 60 K, only very minor changes in the capacitance values were observed. However, at a particular temperature $\approx T = 50$ K, a steep drop in the C_b value can be observed. This effect is related to carrier freeze out, which occurs when the thermal energy is insufficient to ionize the dopant impurity atoms. This phenomenon depends on the dopant energy level in the bandgap, and thus occurs at different temperatures for different impurities. Figure 2a shows that the freezing-induced C_b drop happens at the same temperature in all the samples, and no carrier freezing-induced steps related to dopants other than Ga are present in the $C_b(T)$ curve. This gives confidence in the fact that no significant concentrations of contaminant impurities are present in these samples and that the bulk Ga concentration, deduced from CV measurements, is reliable.

High-resolution, low-temperature PL can also be used to detect residual impurities in Si based on the positions of BE-related peaks, which are different for different acceptor/donor impurities. Figure 2b shows the low-temperature PL spectra from different single-doped Si materials in the BE_{NP} region. The energetic positions of the impurity-related X_{NP} (X = B, P, or Ga) peaks are clearly different. Given that the spectrum for the Ga-doped sample in Figure 1 shows no evidence of either peaks or shoulders at the corresponding energetic positions of the B_{NP} or P_{NP} lines, contamination with B or P, above any residual level, can be ruled out. This provides further confidence in the Ga concentration values deduced from room temperature CV measurements.

2.3. Calibration Curve

It was first noted by Tajima et al.^[20] that at least four different concentrations need to be available to determine reliable

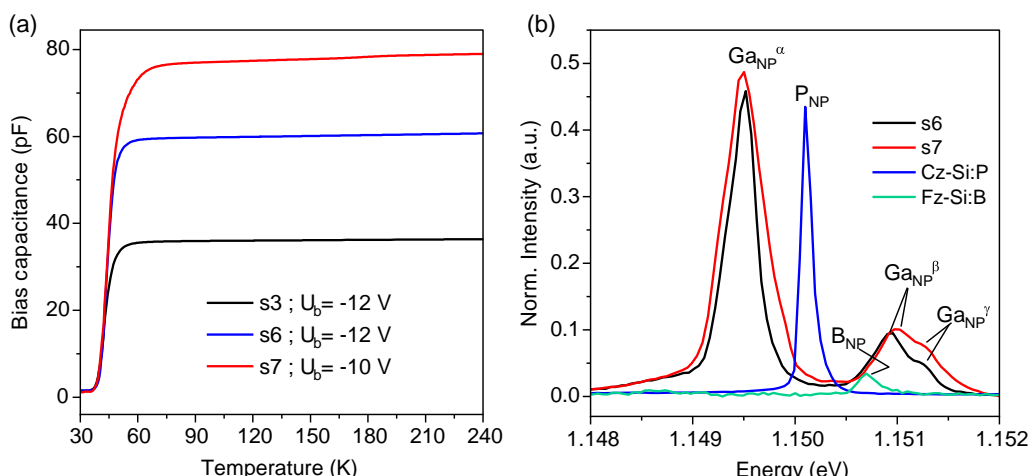


Figure 2. a) Changes in the capacitance of Schottky diodes as a function of temperature for different CCz-Si and FZ-Si samples doped with Ga, measured under similar reverse bias of -10 or -12 V and temperature rise rate of 3 K min^{-1} . b) PL spectra of differently doped Si samples in the energy range 1.148 – 1.152 eV where the principal BE_{NP} lines appear. The spectra were recorded at 10 K.

calibration curves. In this study, we used nine samples with varying doping concentrations, as described in Table 2. The spectrometer was centered at 1110 nm where a single spectrum is recorded using the array detector and optimized to yield the highest intensity of the Ga_{TO}^β peak. With the low dispersion grating we used, it was possible to record the most intense NP line Ga_{NP}^α in the same spectrum without changing the spectrometer center position. This is good practice as moving the grating has the potential to introduce uncertainties in the absolute intensity of the measured PL. After correcting for the system response (in the same wavelength range), the peak intensities of Ga_{TO}^β , Ga_{NP}^α , and FE_{TO} lines were used to deduce the Ga_{TO}^β/FE_{TO} and Ga_{NP}^α/FE_{TO} ratios due to the simplicity of this approach in comparison with others (e.g., the use of area ratio) and its universal use on several materials by different groups (see Table 1). Figure 3 shows the obtained values of the ratios for samples with different Ga concentrations on a log-log scale. To take into account any areal variation in the Ga concentration in the same sample, numerous PL spectra were recorded at different positions on the same sample. These variations are accounted for in Figure 3 by the error bars and the dark/red symbols represent the mode value. Note that the deviation from the mode values is always $<25\%$.

Both sets of data are well described using a linear function and thus serve as calibration curves for accurate determination of the Ga concentration over this range. It is worth highlighting that the calibration line based on the Ga_{NP}^α/FE_{TO} ratio is especially useful, where one might suspect contamination from B. This is because of the energetic overlap of the Ga_{TO}^β peak and the first B-related multiexciton complex, B_{TO}^1 ,^[11] and the fact that the B lines are usually very weak in the NP region,^[36] thus minimizing the error in the method. The calibration of the Ga_{NP}^α/FE_{TO} ratio (red line in Figure 4) is reliable; however, it is important to caveat that the conditions under which the PL spectra were recorded (and used for the calibration) were optimized for the most

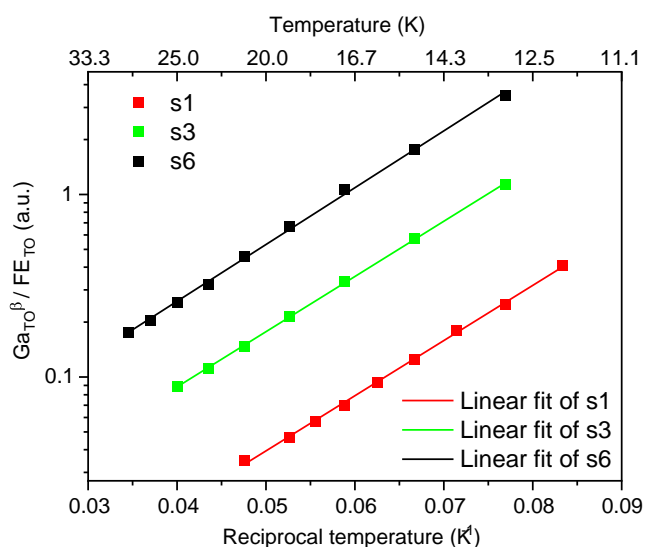


Figure 4. Temperature dependence of Ga_{TO}^β/FE_{TO} intensity ratio for samples s1, s3, and s6.

intense peak (Ga_{TO}^β) in the spectrum rather than the most intense peak in the NP region, i.e., the Ga_{NP}^α peak. If the PL signal is instead optimized for the Ga_{NP}^α peak, deviation from the red calibration curve might be expected and another calibration curve might be required under this specific condition.

2.4. Equation for Calibration Curve

We attempted to deduce the empirical relation between the ratio, the Ga concentration and sample temperature. At a given excitation intensity, the PL peak intensity ratio depends mainly on the acceptor concentration and the sample temperature and can be described as^[23]

$$\frac{\text{Extrinsic component}}{\text{Intrinsic component}} = A \times [Ga]^x \times \exp(y/kT) \quad (1)$$

In order to extract all the parameters (A, x, and y), the determination of the ratio at a specific temperature has to be combined with the temperature dependence behavior of the ratio in samples with different concentrations. The coefficients in Equation (1) can be determined from the fitting of the measured data based on two steps. First, at a given temperature (10 K in this work), the right most term in Equation (1), $\exp(y/kT)$, is constant. This means that the parameter extracted from a linear fit in Figure 3 can be used to extract constants A1 and x. Second, for a given sample with a constant Ga concentration, the ratio will vary with the change in sample temperature, i.e., increasing temperature will result in enhancement of the FE peak and a corresponding reduction of the BE-related peaks, thus the ratio will decrease. In this case, the second term on the right-hand side of Equation (1), $[Ga]^x$, is constant and a linear fit of the data can be used to extract constants A2 and y. Then, the value of constant A will be the product of A1 and A2. Figure 4 shows the

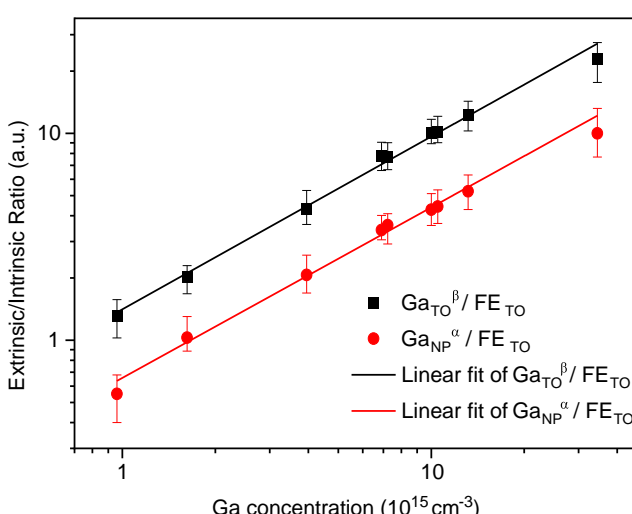


Figure 3. Changes in the extrinsic (Ga_{TO}^β or Ga_{NP}^α) to intrinsic (FE_{TO}) ratio as function of the Ga concentration, deduced from the PL spectra recorded at 10 K. The straight-line fits represent the calibration curve using the PL method for Ga-doped Si.

Table 3. Parameter extracted from fitting data in Figure 3 and 4 for Ga in Si calibration curve.

Ratio from PL	$A = A1 \times A2$	x	y [meV]
Ga_{TO}^β/FE_{TO}	3.7187×10^{-16}	0.835 ± 0.025	6.058 ± 0.203
Ga_{NP}^α/FE_{TO}	2.4719×10^{-16}	0.825 ± 0.035	6.066 ± 0.386

changes in the PL intensity ratio, Ga_{TO}^β/FE_{TO} , as a function of temperature in three different samples on a semilog scale.

The slope and intercept of the linear fits to the data in Figure 4 are used to extract the constants $A2$ and y , respectively. Note that the three samples have approximately the same slope, which reflects the dependence of constant y on the type of acceptor species. A similar set of data was obtained for the Ga_{NP}^α/FE_{TO} ratio.

Combining these two steps, we have determined the values of the three constants A , x , and y as shown in **Table 3**. Inserting these parameters into Equation (1) permits determination of the Ga concentration in Si after PL measurements of the extrinsic/intrinsic ratios in the temperature range 10–25 K. It is found that among the three constants, parameter A varies significantly with Ga concentration, whereas the other two showed only very slight changes, well within the experimental error margins reported in Table 3. Indeed, the $A2$ component of A is responsible for these changes, which was found to increase with increasing Ga concentration. This is in agreement with the increase in the same parameter with the increase in B or P concentration, as reported by Tajima et al.^[23] A universal relation between this parameter and the Ga concentration is yet to be produced and would need the study of a wider range of concentrations. Parameter y is related to the exciton binding energy to the Ga atom, and is in excellent agreement with the values determined by Vouk and Lightowers ($E_{BE(Ga)} = 6.0$ meV)^[37] and with that determined by Haynes ($E_{BE(Ga)} \approx 6.5$ meV).^[38]

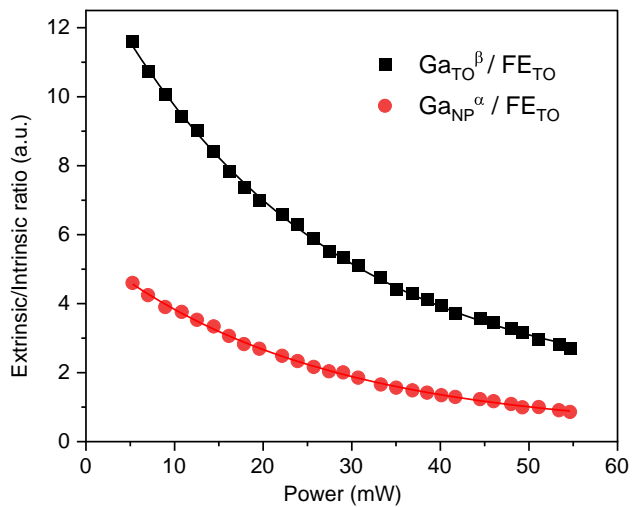
2.5. Power Dependence of PL Intensity Ratio

For one of the studied samples (sample s6), the excitation intensity dependence of the PL intensity ratio was determined. We observed an increase in the intensity of the Ga_{TO}^β , Ga_{NP}^α , and FE_{TO} peaks with increasing excitation power, although we note that this increase was more pronounced for the Ga_{TO}^β peak than for the Ga_{NP}^α peak. The FE_{TO} peak also increases due to the sample heating by the laser spot and the availability of more excitons to go through the intrinsic recombination channel. **Figure 5** shows the changes in the deduced PL intensity ratio as a function of excitation laser power at a starting sample temperature of 10 K.

The data are well described using single exponential decay functions of the form:

$$\frac{\text{Extrinsic component}}{\text{Intrinsic component}} = y_0 + B \times \exp(-P/\rho) \quad (2)$$

where P is the laser excitation power measured at the sample position, and y_0 , B , and ρ are fitting constants. The exponential decrease in Figure 5 reflects the fact that changes in intensity of the FE_{TO} peak on the BE/FE ratios are more pronounced than

**Figure 5.** PL intensity ratio with increasing laser power for sample s6. The lines represent fits to the data using decaying exponential functions.

those for the BE-related peaks, i.e., slight changes in FE_{TO} could yield significant changes in the ratio. This indicates the importance of accurately controlling the sample temperature (which is known to significantly affect the FE-related emission intensity) in order to determine reliable ratios. This has been highlighted very recently in the literature on analysis of low-temperature PL spectra for B-doped Si samples, and a new calibration curve for B in Si has been obtained based on a sophisticated fitting model which distinguishes the FE_{TO} and FE_{LO} peaks for assessment of the actual measurement temperature.^[39]

Table 4 shows the parameters extracted from a single exponential fit of the power-dependent intensity ratio data, shown in Figure 5. Note that the decay constant, ρ , is nearly identical for both ratios. This shows that even though the intensity gain in the Ga_{TO}^β peak is higher than that for Ga_{NP}^α , the decay constant in the ratio due to a more intense excitation is independent of the extrinsic peak chosen, unlike the pre-exponential factor, which is affected by the absolute intensity of the chosen extrinsic peak.

3. Conclusion

The growing importance of Ga as the acceptor impurity of choice in Si-based photovoltaics warrants a deeper understanding of its electronic properties. As such, we have conducted an impurity analysis of this material by way of low-temperature PL spectroscopy to probe samples with varying Ga concentrations. We have confirmed the existence of three BE-related peaks associated with the presence of Ga in Si, as well as confirming negligible

Table 4. Parameters extracted from data fitting in Figure 5 using Equation (2).

Ratio from PL	y_0	B	ρ
Ga_{TO}^β/FE_{TO}	1.4 ± 0.1	12.427 ± 0.072	25.083 ± 0.573
Ga_{NP}^α/FE_{TO}	0.284 ± 0.051	5.28 ± 0.04	25.168 ± 0.689

concentrations of compensating impurities in the samples we studied, key to giving confidence in deriving single impurity properties. PL spectra, all recorded at 10 K, were used to determine the intensity ratio of extrinsic to intrinsic features. The calibration curves for Ga-doped Si based on Ga_{TO}^{β}/FE_{TO} and Ga_{NP}^{α}/FE_{TO} ratios were found by calibrating against the Ga concentration deduced from C–V measurements. By combining the calibration curves for measurements at 10 K with the Arrhenius analysis of the BE/FE ratios in samples with different Ga concentrations, the coefficients in the calibration equations have been determined. Further, excitation power-dependent PL reveals that the intensity ratios are primarily affected by changes in the intensity of the FE_{TO} peak, which is enhanced by local increases in temperature at the laser spot.

4. Experimental Details

The wafers used in this study were cut from Ga-doped Si ingots grown either by the CCz or by the FZ techniques from different producers. Growth conditions were optimized to minimize contamination with any residual impurities. FZ-grown samples were mirror polished on both sides. The segregation coefficient of Ga results in a variation in the doping concentration along the ingot length.

C–V and C–T Measurements: To confirm the presence of only Ga acceptors and to correlate the intensities of PL lines with the Ga concentrations in our samples, C–V and capacitance–temperature (C–T) measurements were used. This was facilitated using high quality Schottky diodes fabricated on small samples cut from the starting wafers. After cleaning of all diced samples, they were dipped in dilute (10%) hydrofluoric (HF) acid to remove the native oxide layer. Samples were then placed in a plasma sputtering chamber where a titanium/Al stack was deposited through a shadow mask to form the Schottky diodes with area $\approx 1.17 \text{ mm}^2$. Subsequently, gold was deposited, via thermal evaporation, on the back-side of the samples to form an Ohmic contact. The processed devices were then mounted on ceramic substrates and wire bonded to facilitate electrical measurements. We assessed the quality of the fabricated diodes via current–voltage ($I – V$) measurements, which revealed a leakage current less than 10^{-6} A at -12 V . C–V measurements were carried out at a frequency of 1 MHz to determine the uncompensated ionized shallow acceptor concentration in the depletion region. On some of the fabricated diodes, measurements of the temperature-dependent bias capacitance were also recorded to probe the possibility of contamination with any compensating/codoping impurities.

C–V measurements can provide a very precise measure of shallow dopant concentration, much more accurate than SIMS for example. The principal source of error arises from uncertainty in the exact area of the test diode. We used a shadow mask with an estimated areal error of $\pm 2\%$, resulting in a possible error in the Ga concentration of $\pm 4\%$. Further improvements in this could be achieved using photolithography, which has the potential to reduce the error in determining the Ga concentration to $< \pm 1\%$.

PL Measurements: Sister samples were cut from the same wafers for PL measurements. Samples with unpolished surfaces were gently etched in a mixture of HF and nitric acid (HF:7HNO₃) for approximately 30 s. This is commonly used to produce a surface with suitable optical quality and to minimize defects, associated with sawing and lapping that can result in considerable surface recombination. Treated samples of the size $10 \times 4 \text{ mm}$ approximately were then mounted, using a thermally conducting silver DAG, on a 1 inch copper disk, which is screwed to the bottom of the cold finger of a Leybold closed-cycle He cryostat. Samples were mounted carefully to avoid spectral contamination from the silver DAG. The cryostat is pumped to achieve a vacuum of $< 10^{-6} \text{ mbar}$, which is maintained for 24 h before the cooling cycle is started. The sample temperature was monitored and controlled using a Si diode and integrated

resistive heater element, mounted at the back of the copper disk, directly behind the samples. An Oxford Instruments ITC4 PID controller provides accurate control and measurements across a large temperature range, from 10 K to room temperature. A second DT670 Lakeshore Si diode is mounted on the front side of the copper disk, adjacent to the samples, and this is connected to a Lakeshore 335 temperature monitor to give an independent temperature reading. The combined reading from both sensors enables accurate determination of (and confidence in) the sample temperature determined during PL measurements. Samples were kept at the minimum temperature for several hours to ensure the actual sample temperature matches the readings from the two sensors. A current controlled 780 nm laser diode with a minimum 8.9 mW pump power, measured at the sample position, was used to excite the samples. Mirrors were used to direct and focus the laser spot (which has an area of $\approx 0.05 \text{ mm}^2$) onto the samples. For samples in good thermal contact with the cryostat cold finger, no appreciable thermal effects are expected for the spectra recorded at low excitation intensity ($\approx 9 \text{ mW}$) we have used.^[40] Power-dependent PL was performed by varying the laser power (at the sample position) from 8.9 to 55 mW.

The emitted PL from the samples was collected, collimated, and focused, using an adjustable two lens, f-number matched optical arrangement, onto a 40 μm entrance slit of an iHR550 Horiba spectrometer. The collected signal is dispersed in the spectrometer using a 600 gr mm^{-1} grating blazed at 1000 nm and detected by a liquid N-cooled InGaAs array. We average the collected spectra over several accumulations to improve the signal to noise ratio. All spectra were corrected for the system response, via measurements of a calibrated ($T = 3000 \text{ K}$) white light source. To rule out the possibility of contamination of common dopant impurities, in our Si test samples, PL spectra were also collected from control B- and P-doped Cz-Si samples with resistivity of $\approx 1 \Omega \text{ cm}$, which were processed in parallel with the Ga-doped samples.

Acknowledgements

This work was supported in the UK by Engineering and Physical Sciences Research Council (EPSRC) project EP/T025131/1.

Conflict of Interest

The authors declare no conflict of interest.

Data Availability Statement

The data that support the findings of this study are available from the corresponding author upon reasonable request.

Keywords

calibration curves, doping concentrations, gallium (Ga), photoluminescence (PL), Si solar cells

Received: November 23, 2023

Revised: December 21, 2023

Published online: January 8, 2024

[1] VDMA, International Technology Roadmap for Photovoltaic (ITRPV), 2023.

[2] N. E. Grant, P. P. Altermatt, T. Niewelt, R. Post, W. Kwapis, M. C. Schubert, J. D. Murphy, *Sol. RRL*. **2021**, 5, 2000754.

- [3] T. O. A. Fattah, J. Jacobs, V. P. Markevich, N. V. Abrosimov, M. P. Halsall, I. F. Crowe, A. R. Peaker, *J. Sci.: Adv. Mater. Devices* **2023**, *8*, 100629.
- [4] M. Tajima, H. Toyota, A. Ogura, *Jpn. J. Appl. Phys.* **2022**, *61*, 080101.
- [5] M. Tajima, *Appl. Phys. Lett.* **1978**, *32*, 719.
- [6] Japanese Industrial Standard, JIS H 0615, **1996**.
- [7] Semiconductor Equipment and Materials International, SEMI MF1389-1115, **2022**.
- [8] American Standards for Testing and Materials, *Annual Book of ASTM Standards*, American Society for Testing and Materials, Philadelphia **1989**.
- [9] J. C. Irvin, *Bell Syst. Tech. J.* **1962**, *41*, 387.
- [10] D. Long, J. Myers, *Phys. Rev.* **1959**, *115*, 1107.
- [11] K. L. Schumacher, R. L. Whitney, *J. Electron. Mater.* **1989**, *18*, 681.
- [12] H. Zimmermann, R. Boyn, C. Michel, P. Rudolph, *Phys. Status Solidi A* **1990**, *118*, 225.
- [13] M. Isshiki, K. Masumoto, W. Uchida, S. Satoh, *Jpn. J. Appl. Phys.* **1991**, *30*, 515.
- [14] M. Allardt, V. Kolkovsky, K. Irmscher, J. Weber, *J. Appl. Phys.* **2012**, *112*, 103701.
- [15] M. A. Reschchikov, M. Vorobiov, O. Andrieiev, K. Ding, N. Izyumskaya, V. Avrutin, A. Usikov, H. Helava, Y. Makarov, *Sci. Rep.* **2020**, *10*, 2223.
- [16] M. Omori, T. Miyazaki, K. Watanabe, M. Shiraishi, R. Wada, T. Okawa, *Appl. Phys. Express* **2021**, *14*, 051002.
- [17] M. Tajima, A. Yusa, T. Abe, *Jpn. J. Appl. Phys.* **1980**, *19*, 631.
- [18] M. Tajima, M. Nomura, *Jpn. J. Appl. Phys.* **1981**, *20*, 297.
- [19] P. M. Colley, E. C. Lightowers, *IOPScience* **1987**, *2*, 157.
- [20] M. Tajima, T. Masui, D. Itoh, T. Nishino, *J. Electrochem. Soc.* **1990**, *137*, 3544.
- [21] A. S. Kaminskii, L. I. Kolesnik, B. M. Leiferov, Y. E. Pokrovskii, *J. Appl. Spectrosc.* **1982**, *36*, 516.
- [22] H. Nakayama, T. Nishino, Y. Hamakawa, *Jpn. J. Appl. Phys.* **1980**, *19*, 501.
- [23] T. Iwai, M. Tajima, A. Ogura, *Physica Status Solidi* **2011**, *8*, 792.
- [24] K. Lauer, C. Möller, D. Schulze, T. Bartel, F. Kirscht, *Phys. Status Solidi Rapid Res. Lett.* **2013**, *7*, 265.
- [25] A. Liu, H. T. Nguyen, D. Macdonald, *Phys. Status Solidi A* **2016**, *213*, 3029.
- [26] M. Tajima, Y. Kamata, *Jpn. J. Appl. Phys.* **2013**, *52*, 086602.
- [27] M. Tajima, S. Samata, S. Nakagawa, Y. Shinozuka, J. Oriyama, N. Ishihara, *Jpn. J. Appl. Phys.* **2021**, *60*, 026501. with corrigendum Tajima et al., *Jpn. J. Appl. Phys.* **2023**, *62*, 089301.
- [28] M. Tajima, S. Samata, S. Nakagawa, J. Oriyama, N. Ishihara, *Jpn. J. Appl. Phys.* **2020**, *59*, SGGK05.
- [29] M. Lax, J. J. Hopfield, *Phys. Rev.* **1961**, *124*, 115.
- [30] M. L. W. Thewalt, *Phys. Rev. Lett.* **1977**, *38*, 521.
- [31] M. L. W. Thewalt, *Can. J. Phys.* **1977**, *55*, 1463.
- [32] T. O. Abdul Fattah, J. Jacobs, V. P. Markevich, N. V. Abrosimov, M. P. Halsall, I. F. Crowe, A. R. Peaker, presented at *50th IEEE Photovolt. Spec. Conf. (PVSC 50)*, Puerto Rico, June, **2023**.
- [33] G. Davies, *Phys. Rep.* **1989**, *176*, 83.
- [34] E. C. Lightowers, M. O. Henry, *J. Phys. C: Solid State Phys.* **1977**, *10*, 247.
- [35] M. Tajima, G. Kato, K. Nakagawa, F. Higuchi, A. Ogura, presented at *15th Int. Workshop on Junction Technol. (IWJT)*, IEEE, Kyoto, Japan, June **2015**, pp. 34–39.
- [36] K. Kosai, M. Gershcnzon, *Phys. Rev. B* **1974**, *9*, 723.
- [37] M. A. Vouk, E. C. Lightowers, *J. Lumin.* **1977**, *15*, 357.
- [38] J. R. Haynes, *Phys. Rev. Lett.* **1960**, *4*, 361.
- [39] K. Peh, A. Flötotto, K. Lauer, D. Schulze, D. Bratek, S. Krischok, *Phys. Status Solidi B* **2023**, *260*, 2300300.
- [40] I. Pelant, J. Dian, J. Matoušková, J. Valenta, J. Hála, M. Ambrož, M. Vácha, V. Kohlová, K. Vojtěchovský, K. Kašík, *J. Appl. Phys.* **1993**, *73*, 3477.
- [41] A. Y. Liu, H. T. Nguyen, D. Macdonald, *IEEE J. Photovolt.* **2017**, *7*, 581.